Drying Technology: An International Journal

Numerical Analysis of Heat–Mass Transport and Pressure Build-Up in 1D Unsaturated Porous Medium Subjected to a Combined Microwave and Vacuum System

K. Chaiyo [a] & P. Rattanadecho [a]

[a] Research Center of Microwave Utilization in Engineering, Department of Mechanical Engineering, Faculty of Engineering , Thammasat University , Patumthani , Thailand
Published online: 28 Apr 2013.

PLEASE SCROLL DOWN FOR ARTICLE

Taylor & Francis
Taylor & Francis Group

Numerical Analysis of Heat–Mass Transport and Pressure Build-Up in 1D Unsaturated Porous Medium Subjected to a Combined Microwave and Vacuum System

K. Chaiyo and P. Rattanadecho

Research Center of Microwave Utilization in Engineering, Department of Mechanical Engineering, Faculty of Engineering, Thammasat University, Patumthani, Thailand

This article presents one-dimensional numerical analysis of heat-mass transport and pressure build-up inside an unsaturated porous media under microwave energy at a vacuum pressure condition. The unsaturated porous media is composed of glass beads, water, and air. The absorbed microwave power term is computed based on Lambert's law. The finite difference method together with Newton-Raphson technique is employed to predict the heat, multiphase flow, and pressure build-up. Based on the numerical analysis of the effects of vacuum pressure and types of dielectric materials, it was found that the vacuum pressure had a strong effect on temperature, absorbed microwave power, saturation and pressure build-up distribution, and movement of fluid inside the unsaturated porous media during the microwave drying process.

INTRODUCTION

Microwave technology has been applied to many drying processes for several decades. In microwave drying, that heat is generated by directly transforming the electromagnetic energy into kinetic energy, thus heat is generated deep within the material to be dried. Some of the successful examples of microwave drying are in a ceramics process for drying and sintering, drying of paper, freeze drying, and vulcanization of rubber. Furthermore, excellent reviews of microwave drying are presented by Mujumdar,[1] Metaxas and Meridith,[2] Datta and Anantheswaran.[3] In vacuum drying, processes can offer reduced drying times and higher end-product quality in comparison with a conventional drying.[4,5] Indeed, operating at low pressure reduces the boiling point of water, and provides low temperature to treat product throughout the drying process. Vacuum drying is well known in the metallurgical industries for processing of high purity alloys. It is apparent that microwaves can provide a substantial increase rate of heating in a vacuum environment compared with other methods. However, it may be limited not only by the usual restraint of mass transfer but also by the onset breakdown electric filed. Fundamental to the operation of a vacuum drying system is the operating pressure to control the temperature of the product below a prescribed limit. Figure 1 shows the boiling point temperature of water versus pressure range of 1–133 kPa (about 0.1–1000 torr). For vacuum drying, the pressure range of 1.33–26.6 kPa (about 10–200 torr) is a more successful application to drying heat-sensitive materials such as pharmaceutical products and other chemicals. The critical breakdown electric field should also be carefully selected to avoid breakdown electric field responses causing the effect of breakdown in gas such as air or water vapor.[2]

Microwave vacuum drying provides higher product qualities and an improved drying rate compared to conventional drying processing by experimental investigations of many researchers. Some of the successful research of experimental microwave vacuum drying has been as follows. Drouzas and Schubert[6] investigated experimentally microwave vacuum dying of banana slices that dehydrated products of excellent quality as examined by taste, color, aroma, smell, and rehydration tests compared to conventional drying. Drouzas et al.[7] used a laboratory microwave vacuum drier to investigate drying kinetics experiments with model fruit gel, simulating orange juice concentrate in which the drying rate constant of the thin-layer drying model is increased with increasing microwave power output and decreasing absolute pressure in vacuum drying. Péré and Rodie[8] presented experimental results obtained by microwave vacuum drying of a package of initially water-saturated glass beads and a package of initially unsaturated pharmaceutical granules. Sunjka et al.[9] investigated two drying methods of cranberries, microwave-vacuum and microwave-convective, in which microwave vacuum drying exhibited enhanced characteristics in almost all observed parameters (color, textural

Correspondence: P. Rattanadecho, Research Center of Microwave Utilization in Engineering (RCME), Department of Mechanical Engineering, Faculty of Engineering, Thammasat University (Rangsit Campus), Patumthani 12120, Thailand; E-mail: ratphadu@engr.tu.ac.th
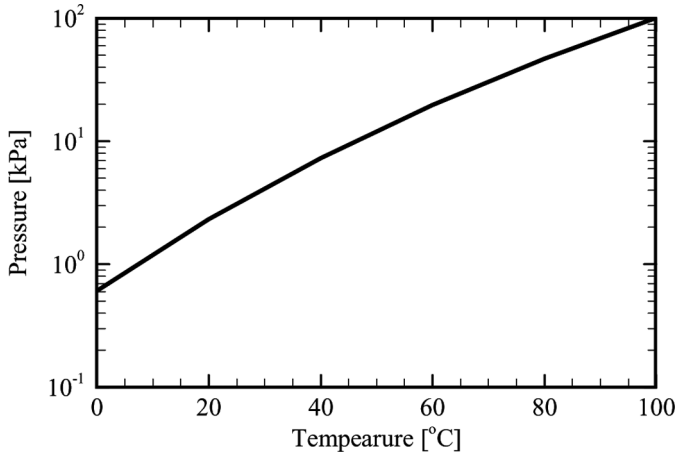
FIG. 1.   Saturation vapor pressure of water as a function of temperature.

characteristics, organoleptic properties) and was more energy-efficient when compared to microwave-convective drying. Hu et al.[10] compared the characteristics of hot-air and microwave-vacuum combination drying using edamame as the raw material; it was found that combined hot air and microwave vacuum are able to increase drying rate and enhance product quality.

In a theoretical analysis, heat and mass transfer in porous materials were studied for several decades and can be classified into three different fundamentals as follows.

1. The single variable model: one diffusion equation of moisture content is used for simple configuration.
2. The two variables model: two dependent variables as temperature and moisture content are employed, and effect of pressure build-up can be neglected.
3. The three variables model: three dependent variables (temperature, moisture content, and pressure build-up) are used; this model provides better transport phenomena details than other models.

The single-variable and two-variables models are mostly applied to investigate conventional drying because they are not complicated by a manipulated numerical scheme. However, studies using the three-variables model are Datta and Anantheswaran,[3] Perré and Turner,[11] Rattanadecho et al.,[12] and Ni et al.[13]

A few researchers have numerically studied heat and mass transport phenomena of porous material under microwave drying processing, and most previous works have not mentioned pressure build-up within porous material.[14–19] Some previous researchers (Sungsoontorn et al.[20] and Suwannapum et al.[21]) revealed pressure build-up by using the three-variables model for microwave drying of an unsaturated porous media. However, the numerical studies in the case of microwave vacuum drying of unsaturated porous media have not been investigated before. Therefore, this research studies the influence of

vacuum pressure and material properties of solid particles to affect internal phenomena of unsaturated porous medium when applying microwave energy.

The present paper introduces the numerical approach to investigate heat–mass transport and pressure build-up phenomena during the vacuum drying process in a uniform, porous, packed bed (as sample) under microwave energy. In an analysis, absorbed microwave power is assumed to decay exponentially into the sample following Lambert's law. The objective of this study is carried out to predict temperature, absorbed microwave power, pressure build-up distributions, and moisture profiles at vacuum and atmospheric pressure. Furthermore, the influence of material properties is investigated.

RELATED THEORIES

A one-dimensional model of the analytical model for microwave vacuum drying of the sample is schematically shown in Fig. 2. The sample is an unsaturated porous medium and is assumed to be a non-hygroscopic porous medium that is homogeneous, isotropic, and reproducible. It is composed of solid particles (glass beads), water, and air. The rate of volumetric energy absorbed corresponding to the absorbed microwave power is assumed to decay exponentially into the sample according to Lambert's law. The basic equation to calculate the density of absorbed microwave power by dielectric material can be written in the final form as[20,22]:

$$Q = -\frac{\partial P}{\partial z} dz = 2\alpha P dz = 2\alpha dz \cdot 2\pi f \varepsilon' (\tan \delta) E^2 e^{-2\alpha z}$$

(1)

where E is the electromagnetic field intensity, f is the frequency of the microwave, $\tan \delta$ is the dielectric loss tangent coefficient, and α is the attenuation constant, which can be
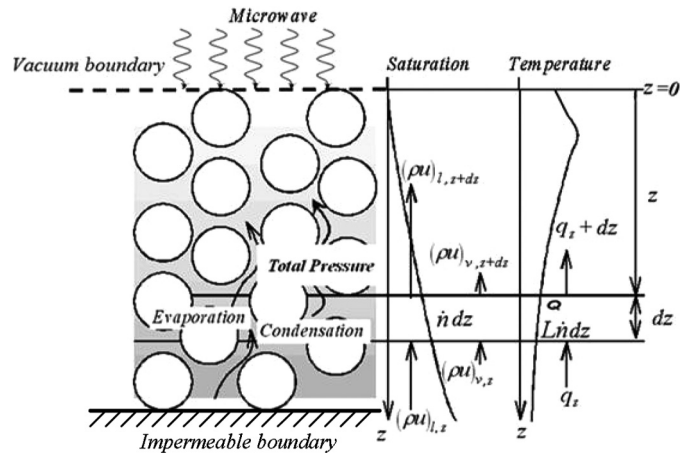

FIG. 2.   Analytical model of the sample exposed to microwave irradiation.

calculated as:

$$\alpha = \frac{2\pi f}{c} \sqrt{\frac{\varepsilon'_r}{2} \left(\sqrt{\tan^2 \delta + 1} - 1 \right)} \qquad (2)$$

The attenuation parameter controls the rate at which the incident field decays, and is inversely proportional to the skin depth ($\alpha = 1/\delta_s$). In this work, the effects of the overall drying kinetics are examined by selecting the dielectric properties as a function of water saturation (moisture content) and temperature. In order to determine the functional dependence of the combination of moisture content and temperature, the theory surrounding mixing formulas is used, in which the volume fractions (v) of water saturation, vapor, and glass beads is considered, as follows[14,22]:

$$\varepsilon(s, T) = \varepsilon'(s, T) - j\varepsilon''(s, T) \qquad (3)$$

where

$$[\varepsilon'(s, T)]^m = \sum_{i=1}^{3} v_i [\varepsilon'_{ri}(T)]^m = \phi \cdot s[\varepsilon'_{rl}(T)]^m$$
$$+ \phi(1-s)[\varepsilon'_{ra}]^m + (1-\phi)[\varepsilon'_{rp}]^m \qquad (4)$$

$$[\varepsilon''(s, T)]^m = \sum_{i=1}^{3} v_i [\varepsilon''_i(T)]^m = \phi \cdot s[\varepsilon''_{rl}(T)]^m$$
$$+ \phi(1-s)[\varepsilon''_{ra}]^m + (1-\phi)[\varepsilon''_{rp}]^m \qquad (5)$$

in which the parameter m is likely to vary over the range $0 - 1$, as suggested by Wang and Schmugge.[23] The loss tangent coefficient can be expressed as follows:

$$\tan \delta = \frac{\varepsilon''}{\varepsilon'} \qquad (6)$$

where ε' is a dielectric constant and ε'' is a dielectric loss factor.

The dielectric properties of water taken from Von Hippe[24] are a function of temperature. The dielectric properties of gas are assumed to be constant. The numerical values for skin depth, relative permittivity, and loss tangent at various moisture contents for present study are listed in Table 1.

In this analysis, the main transport mechanisms that enable moisture movement during the microwave drying of the sample are liquid flows driven by capillary pressure gradient and gravity. However, the vapor is driven by the gradient of the partial pressure of the evaporating species. The main assumptions involved in the formulation of the transport model are:

1. The unsaturated porous material is rigid and chemical reactions did not occur in the sample.

TABLE 1
Dielectric properties of the sample (corresponding to: T = 20[°C] and f = 2.45 GHz)[22]

Moisture content (s)	Relative permittivity (ε'_r)	Loss tangent (tan δ)	Skin depth (δ_s)
0.00	3.5420	0.0062	3.338119
0.25	10.9606	0.0190	0.607039
0.50	18.3110	0.0319	0.285429
0.75	25.6955	0.0447	0.171784
1.00	33.0801	0.0589	0.117645

2. The local thermodynamics equilibrium among each phase is assumed.
3. The gas phase is ideal in the thermodynamic sense.
4. The contribution of convection to energy transport is included.
5. Darcy's law holds valid for the liquid phase and gas phase.
6. Gravity is included, particularly in the liquid phase and gas phase.
7. The permeability of liquid and gas can be expressed in terms of relative permeability.
8. In a macroscopic sense, the sample is assumed to be homogeneous and isotropic, and liquid water is not bound to the solid matrix. Therefore, the volume average model for a homogeneous and isotropic material can be used in the theoretical model and analysis.
9. Corresponding to the electric field, the temperature and moisture profiles are assumed to be in one-dimensional form.
10. The non-thermal effect of microwave irradiation is neglected.

Mass Conservation

The macroscopic mass conservation equations for liquid, vapor, and air phase are written, respectively, as:

Liquid phase $\quad \rho_l \phi \dfrac{\partial s}{\partial t} + \rho_l \dfrac{\partial u_l}{\partial z} = -n \qquad (7)$

Vapor phase $\quad \dfrac{\partial}{\partial t}[\rho_v \phi(1-s)] + \dfrac{\partial}{\partial z}(\rho_v u_v) = n \qquad (8)$

Air phase $\quad \dfrac{\partial}{\partial t}[\rho_a \phi(1-s)] + \dfrac{\partial}{\partial z}(\rho_a u_a) = 0 \qquad (9)$

where n is the condensation rate or the evaporation rate during a phase change. The vapor and air mass flux is the sum of the convective term with the gas superficial velocity and diffusive term. Additionally, the gas phase is assumed to be an ideal mixture of air and vapor phase.

Energy Conservation

The temperature of the sample exposed to irradiation is obtained by solving the conventional heat transport equation with the absorbed microwave power included as a local heat-generation term. The governing energy equation describing the temperature rise in the sample is the time-dependent equation as:

$$\rho\, C_p \frac{\partial T}{\partial t} + \frac{\partial}{\partial z}\left\{\left[\rho_l C_{pl} u_l + (\rho_a C_{pa} + \rho_v C_{pv})\, u_g\right] T\right\} + H_v\, n = \frac{\partial}{\partial z}\left(\lambda_{eff}\frac{\partial T}{\partial z}\right) + Q \tag{10}$$

Phenomenological Relations

In order to complete the system of equations, the expressions for the superficial average velocity of the liquid and gas phase, the generalized Darcy's law in the following form, is used by Ratanadecho et al.[22]:

$$u_l = -\frac{KK_{rl}}{\mu_l}\left[\frac{\partial p_g}{\partial z} - \frac{\partial p_c}{\partial z} - \rho_l g\right] \tag{11}$$

$$u_g = -\frac{KK_{rg}}{\mu_g}\left[\frac{\partial p_g}{\partial z} - \rho_g g\right] \tag{12}$$

where μ_l and μ_g denote the viscosity of liquid and gas phases, respectively. The capillary pressure p_c is related to the gas and liquid phase, and can be written as:

$$p_c = p_g - p_l \tag{13}$$

For the velocity of vapor and air phase, the generalized Fick's law in the following form is used as:

$$\rho_v u_v = \rho_v u_g - \rho_g D_m \frac{\partial}{\partial z}\left(\frac{\rho_v}{\rho_g}\right) \tag{14}$$

$$\rho_a u_a = \rho_a u_g - \rho_g D_m \frac{\partial}{\partial z}\left(\frac{\rho_a}{\rho_g}\right) \tag{15}$$

and D_m is the effective molecular mass diffusion[25] as:

$$D_m = \frac{2\phi}{3 - \phi}(1 - s)D \tag{16}$$

where D is binary mass diffusion in plain media and can be defined as:

$$D = D_0\left(\frac{p_0}{p}\right)\left(\frac{T}{T_0}\right)^{2.2} \tag{17}$$

Equilibrium Relations

The system of conservation equations obtained for multiphase transport mode requires a constitutive equation for a relative liquid permeability K_{rl}, and a relative gas permeability K_{rg}. A typical set of constitutive relationships for liquid and gas system is given by Ratanadecho et al.[22]:

$$K_{rl} = s_e^3 \tag{18}$$

$$K_{rg} = (1 - s_e)^3 \tag{19}$$

where s_e is the effective water saturation considered the irreducible water saturation ($s_{ir} = 0.06$) and defined by:

$$s_e = \frac{s - s_{ir}}{1 - s_{ir}} \tag{20}$$

The capillary pressure is further assumed to be adequately represented by well-known Leverett's $J(s_e)$ functions; the relationship between the capillary pressure and the water saturation is defined by using Leverett functions $J(s_e)$ as:

$$p_c = p_g - p_l = \frac{\sigma}{\sqrt{K/\phi}} J(s_e) \tag{21}$$

where σ is the gas-liquid interfacial tension, and Leverett functions are given by:

$$J(s_e) = 0.325(1/s_e - 1)^{0.217} \tag{22}$$

Figure 3 shows the typical moisture characteristic curve (the relationship between capillary pressure and water saturation) for different particle sizes obtained from Ratanadecho et al.[22] It can be seen that, in the case of the same water saturation, a small particle size corresponds to a higher capillary pressure. The characteristics of water transport in porous material obtained here are shown in Table 2.
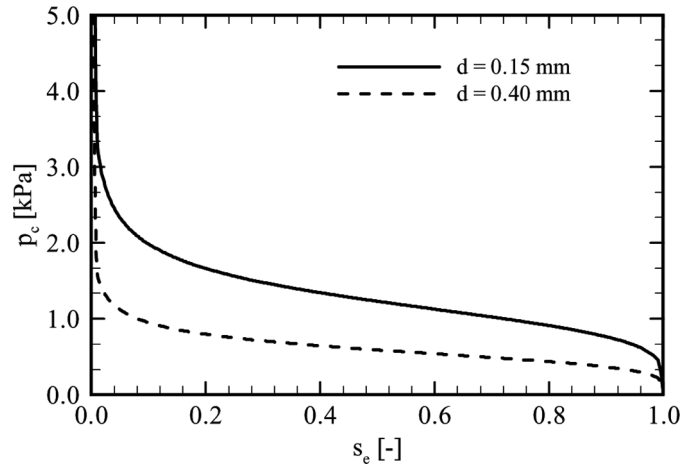

FIG. 3. Typical relationship between p_c and s_e.

The characteristic of water transport in porous material[22]

Diameter, d [mm]	Porosity, ϕ [-]	Permeability, K [m^2]
0.15	0.385	8.41×10^{-12}
0.40	0.371	3.52×10^{-11}

The effective thermal conductivity of the unsaturated porous medium in the case of glass beads is a function of water saturation that can be written as:

$$\lambda_{eff} = \frac{0.8}{1 + 3.78 e^{-5.95s}} \tag{23}$$

In the case of a solid particle, alumina, the effective thermal conductivity[26] is defined by

$$\lambda_{eff} = \lambda_{eff,g} + \sqrt{s} \cdot (\lambda_{eff,l} - \lambda_{eff,g}) \tag{24}$$

where

$$\lambda_{eff,l} = \lambda_l^{\phi} \cdot \lambda_p^{1-\phi} \tag{25}$$

$$\lambda_{eff,g} = \lambda_g^{\phi} \cdot \lambda_p^{1-\phi} \tag{26}$$

Equations of State

The gas phase is assumed to be an ideal mixture of air and vapor, so the density of each phase can be determined by the equations of state:

$$
\begin{aligned}
\rho_a &= \frac{p_a M_a}{R_0 T}, \quad \rho_v = \frac{p_v M_v}{R_0 T} \\
\rho_g &= \rho_a + \rho_v \\
p_a &= \rho_a R_a T, \quad p_v = \rho_v R_v T \\
p_g &= p_a + p_v \\
\rho_g u_g &= \rho_a u_g + \rho_v u_v
\end{aligned} \tag{27}
$$

The partial pressure of vapor is given by Kelvin's equation, based on the capillary force as defined by:

$$p_v = p_{vs} \exp\left(\frac{p_c}{\rho_l R_v T}\right) \tag{28}$$

where p_{vs} is the partial pressure of the saturation vapor as a function of temperature[14,27] that is shown in Fig. 1 and is defined by:

$$p_{vs} = C_0 + C_1 T + C_2 T^2 + C_3 T^3 + C_4 T^4 + C_5 T^5 \tag{29}$$

where

$$C_0 = 610.8, \quad C_1 = 43.87, \quad C_2 = 1.47, \quad C_3 = 0.025.$$
$$C_4 = 2.88 \times 10^{-4}, \quad C_5 = 2.71 \times 10^{-6}.$$

Heat Transport Equation

The kinetic energy and pressure terms, which are usually unimportant, are ignored. Local thermodynamics equilibrium among all phases is assumed. The temperature of unsaturated porous media is obtained by solving the conventional heat transport equation. Considering the enthalpy transport based on the water and gas flows, the conduction heat and latent heat transfer are due to evaporation. The energy conservation equation is represented by:

$$
\begin{aligned}
\rho\, C_p \frac{\partial T}{\partial t} + \frac{\partial}{\partial z} &\left\{ \left[\rho_l C_{pl} u_l + (\rho_a C_{pa} + \rho_v C_{pv}) u_g \right] T \right\} \\
&= \frac{\partial}{\partial z}\left(\lambda_{eff} \frac{\partial T}{\partial z} \right) - H_v \Bigg\{ \frac{\partial}{\partial t}[\rho_v \phi (1-s)] \\
&\quad + \frac{\partial}{\partial z}\left[\rho_v \frac{KK_{rg}}{\mu_g}\left(-\frac{\partial p_g}{\partial z} + \rho_g g_z \right) \right. \\
&\quad \left. - \rho_g D_m \frac{\partial}{\partial z}\left(\frac{\rho_v}{\rho_g} \right) \right] \Bigg\} + Q
\end{aligned} \tag{30}
$$

where

$$\rho\, C_p = \rho_l C_{pl}\, \phi\, s + \left[\rho_a C_{pa} + \rho_v C_{pv} \right] \phi (1-s) + \rho_p C_{pp}(1-\phi).$$

Mass Transport Equation

The phenomenon of moisture transport in the sample is described by the mass conservation equations for the liquid phase and the vapor portion of the gas phase since the total water content is of interest. The addition of those one-dimensional equations (Eqs. (7) and (8)) yields total moisture content as follows:

$$
\begin{aligned}
\phi \frac{\partial}{\partial t}[\rho_l s + \rho_v(1-s)] &+ \frac{\partial}{\partial z}\left[\rho_l \frac{KK_{rl}}{\mu_l}\left(\frac{\partial p_c}{\partial z} - \frac{\partial p_g}{\partial z} + \rho_l g_z \right) \right. \\
&\left. + \rho_v \frac{KK_{rg}}{\mu_g}\left(-\frac{\partial p_g}{\partial z} + \rho_g g_z \right) - \rho_g D_m \frac{\partial}{\partial z}\left(\frac{\rho_v}{\rho_g} \right) \right] = 0
\end{aligned} \tag{31}
$$

The Pressure Build-Up in Porous Media Equation

The pressure build-up in the porous media is obtained from an air-balance equation (Eq. (9)), as follows:

$$
\begin{aligned}
\phi \frac{\partial}{\partial t}[\rho_a(1-s)] &+ \frac{\partial}{\partial z}\left[\rho_a \frac{KK_{rg}}{\mu_g}\left(-\frac{\partial p_g}{\partial z} + \rho_g g_z \right) \right. \\
&\left. - \rho_g D_m \frac{\partial}{\partial z}\left(\frac{\rho_a}{\rho_g} \right) \right] = 0
\end{aligned} \tag{32}
$$

Boundary and Initial Conditions

At open boundary (as vacuum boundary), the liquid and vapor flux reaching the boundary from the interior is fully evaporated and convected away as vapor to the ambient. Regardless of the volumetric evaporation rate inside, any remaining liquid flux arriving at the surface is evaporated at the open boundary. The exchange of energy at the open boundary can be described in the following form:

$$-\lambda_{eff}\frac{\partial T}{\partial z} = h_c(T - T_\infty) + n\,H_v \qquad (33)$$

where h_c is the local heat transfer coefficient.

Mass transfer at the open boundary is modeled by means of a locally constant mass transfer coefficient, which is related to the local water vapor flux density described as:

$$\rho_l u_l + \rho_v u_v = h_m(\rho_v - \rho_\infty) \qquad (34)$$

where h_m is the mass transfer coefficient, ρ_v is the density of vapor at the open boundary, and ρ_∞ is reference vapor density in the gas phase surrounding the open boundary, and assuming in this case the analogy between heat and mass transfer, in which the local mass transfer coefficient h_m can be expressed as[25]:

$$h_m = \frac{h_c}{\rho_g C_{pg} Le^{2/3}} \qquad (35)$$

where

$$Le = \frac{\alpha_g}{D} \qquad (36)$$

The total pressure at open boundary is fixed pressure boundary, p_b, as:

$$p_g = p_b \qquad (37)$$

where p_b is equal to or less than 101.325 kPa in the case of atmospheric pressure and vacuum pressure, respectively.

The boundary conditions at the impermeable boundary where no heat and mass exchange take place are given by:

$$\frac{\partial T}{\partial z} = 0 \qquad (38)$$

$$u = 0 \qquad (39)$$

The initial conditions are uniform initial temperature and moisture in the case with gravitational force.

NUMERICAL PROCEDURE

The system of nonlinear partial differential equations (Eqs. (30)–(32)) must be solved by the method of finite differences based on the notation of control volume as described by Patankar.[28] At each time increment, the nodal values of s, T, and p_g were solved iteratively and the convergence was checked on three variables. The Newton-Raphson method was employed at each iteration to improve the convergence rate. The discretized form of the heat transport equation (Eq. (30)) is given by:

$$
\begin{aligned}
&\frac{(\rho\,C_p)_k^{n+1}T_k^{n+1} - (\rho\,C_p)_k^n T_k^n}{\Delta t} + \frac{\rho_l\,C_{pl}}{\Delta z}(u_{lk}^{n+1}T_k^{n+1} \\
&- u_{lk-1}^{n+1}T_{k-1}^{n+1}) + \frac{\rho_a\,C_{pa} + \rho_v\,C_{pv}}{\Delta z}(u_{gk}^{n+1}T_k^{n+1} \\
&- u_{gk-1}^{n+1}T_{k-1}^{n+1}) - \frac{1}{\Delta z}\left(\lambda_{eff,k+\frac12}^{n+1}\left(\frac{T_{k+1}^{n+1} - T_k^{n+1}}{\Delta z}\right)\right. \\
&\left. - \lambda_{k-\frac12}^{n+1}\left(\frac{T_k^{n+1} - T_{k-1}^{n+1}}{\Delta z}\right)\right) + \frac{H_v\rho_v\phi}{\Delta t}((1-s_{ir})(s_{ek}^{n+1} - s_{ek}^n)) \\
&- \frac{1}{\Delta z}\left(
\begin{array}{l}
\left(\rho_{vk}^{n+1}\left.\frac{KK_{rg}}{\mu_g}\right|_{k+\frac12}^{n+1}\left(-\left(\frac{p_{gk+1}^{n+1}-p_{gk}^{n+1}}{\Delta z}\right)+\rho_g g_z\right)\right. \\
\left.-\rho_{vk-1}^{n+1}\left.\frac{KK_{rg}}{\mu_g}\right|_{k-\frac12}^{n+1}\left(-\left(\frac{p_{gk}^{n+1}-p_{gk-1}^{n+1}}{\Delta z}\right)+\rho_g g_z\right)\right) \\
-\left(\rho_{gk}^{n+1}\left.D_m\right|_{k+\frac12}^{n+1}\left(\frac{\left(\frac{\rho_v}{\rho_g}\right)_{k+1}^{n+1}-\left(\frac{\rho_v}{\rho_g}\right)_k^{n+1}}{\Delta z}\right)\right. \\
\left.-\rho_{gk-1}^{n+1}\left.D_m\right|_{k-\frac12}^{n+1}\left(\frac{\left(\frac{\rho_v}{\rho_g}\right)_k^{n+1}-\left(\frac{\rho_v}{\rho_g}\right)_{k-1}^{n+1}}{\Delta z}\right)\right)
\end{array}
\right) \\
&- Q = 0
\end{aligned}
$$
$$(40)$$

Similarly, the discretized form of mass transport equation (Eq. (31)) can be written as

$$
\begin{aligned}
&\frac{\phi}{\Delta t}(1-s_{ir})[\rho_l(s_{ek}^{n+1}-s_{ek}^n) + (\rho_{vk}^{n+1}(1-s_{ek}^{n+1}) - \rho_{vk}^n(1-s_{ek}^n))] \\
&+\frac{1}{\Delta z}\left(
\begin{array}{l}
\left(\rho_l\left.\frac{KK_{rl}}{\mu_l}\right|_{k+\frac12}^{n+1}\left(\left(\frac{p_{ck+1}^{n+1}-p_{ck}^{n+1}}{\Delta z}\right)-\left(\frac{p_{gk+1}^{n+1}-p_{gk}^{n+1}}{\Delta z}\right)+\rho_l g_z\right)\right. \\
\left.-\rho_l\left.\frac{KK_{rl}}{\mu_l}\right|_{k-\frac12}^{n+1}\left(\left(\frac{p_{ck}^{n+1}-p_{ck-1}^{n+1}}{\Delta z}\right)-\left(\frac{p_{gk}^{n+1}-p_{gk-1}^{n+1}}{\Delta z}\right)+\rho_l g_z\right)\right) \\
+\rho_{vk}^{n+1}\left(\left.\frac{KK_{rg}}{\mu_g}\right|_{k+\frac12}^{n+1}\left(-\left(\frac{p_{gk+1}^{n+1}-p_{gk}^{n+1}}{\Delta z}\right)+\rho_{gk}^{n+1}g_z\right)\right. \\
\left.-\left.\frac{KK_{rg}}{\mu_g}\right|_{k-\frac12}^{n+1}\left(-\left(\frac{p_{gk}^{n+1}-p_{gk-1}^{n+1}}{\Delta z}\right)+\rho_{gk}^{n+1}g_z\right)\right) \\
-\rho_{gk}^{n+1}\left(\left.D_m\right|_{k+\frac12}^{n+1}\left(\frac{\rho_{vk+1}^{n+1}-\rho_{vk}^{n+1}}{\Delta z}\right)-\left.D_m\right|_{k-\frac12}^{n+1}\left(\frac{\rho_{vk}^{n+1}-\rho_{vk-1}^{n+1}}{\Delta z}\right)\right)
\end{array}
\right) \\
&= 0
\end{aligned}
$$
$$(41)$$

The discretized form of the pressure build-up in the porous media equation (Eq. (32)) can also be written as:

$$
\begin{aligned}
&\frac{\phi}{\Delta t}\left[(1-s_{ir})(\rho_{ak}^{n+1}(1-s_{ek}^{n+1})-\rho_{ak}^{n}(1-s_{ek}^{n}))\right] \\
&+\frac{1}{\Delta z}\left(
\begin{array}{l}
\rho_{ak}^{n+1}\left(\frac{KK_{rg}}{\mu_g}\bigg|_{k+\frac{1}{2}}^{n+1}\left(-\left(\frac{p_{gk+1}^{n+1}-p_{gk}^{n+1}}{\Delta z}\right)+\rho_{kg}^{n+1}g_z\right)\right) \\
-\frac{KK_{rg}}{\mu_g}\bigg|_{k-\frac{1}{2}}^{n+1}\left(-\left(\frac{p_{gk}^{n+1}-p_{gk-1}^{n+1}}{\Delta z}\right)+\rho_{kg}^{n+1}g_z\right) \\
-\rho_{gk}^{n+1}\left(D_m\bigg|_{k+\frac{1}{2}}^{n+1}\left(\frac{\left(\frac{\rho_a}{\rho_g}\right)_{k+1}^{n+1}-\left(\frac{\rho_a}{\rho_g}\right)_{k}^{n+1}}{\Delta z}\right)\right) \\
-D_m\bigg|_{k-\frac{1}{2}}^{n+1}\left(\frac{\left(\frac{\rho_a}{\rho_g}\right)_{k}^{n+1}-\left(\frac{\rho_a}{\rho_g}\right)_{k-1}^{n+1}}{\Delta z}\right)
\end{array}
\right)=0
\end{aligned}
$$

(42)

where

$$
\lambda_{eff,k+\frac{1}{2}}^{n+1}=\frac{\lambda_{eff,k}^{n+1}+\lambda_{eff,k+1}^{n+1}}{2} \tag{43}
$$

$$
\lambda_{eff,k+\frac{1}{2}}^{n+1}=\frac{\lambda_{eff,k}^{n+1}+\lambda_{eff,k-1}^{n+1}}{2} \tag{44}
$$

$$
KK_{rg}\big|_{k+\frac{1}{2}}^{n+1}=\frac{KK_{rg}\big|_{k}^{n+1}+KK_{rg}\big|_{k+1}^{n+1}}{2} \tag{45}
$$

$$
KK_{rg}\big|_{k-\frac{1}{2}}^{n+1}=\frac{KK_{rg}\big|_{k}^{n+1}+KK_{rg}\big|_{k-1}^{n+1}}{2} \tag{46}
$$

$$
KK_{rl}\big|_{k+\frac{1}{2}}^{n+1}=\frac{KK_{rl}\big|_{k}^{n+1}+KK_{rl}\big|_{k+1}^{n+1}}{2} \tag{47}
$$

$$
KK_{rl}\big|_{k-\frac{1}{2}}^{n+1}=\frac{KK_{rl}\big|_{k}^{n+1}+KK_{rl}\big|_{k-1}^{n+1}}{2} \tag{48}
$$

$$
D_m\big|_{k+\frac{1}{2}}^{n+1}=\frac{D_m\big|_{k}^{n+1}+D_m\big|_{k+1}^{n+1}}{2} \tag{49}
$$

$$
D_m\big|_{k-\frac{1}{2}}^{n+1}=\frac{D_m\big|_{k}^{n+1}+D_m\big|_{k-1}^{n+1}}{2} \tag{50}
$$
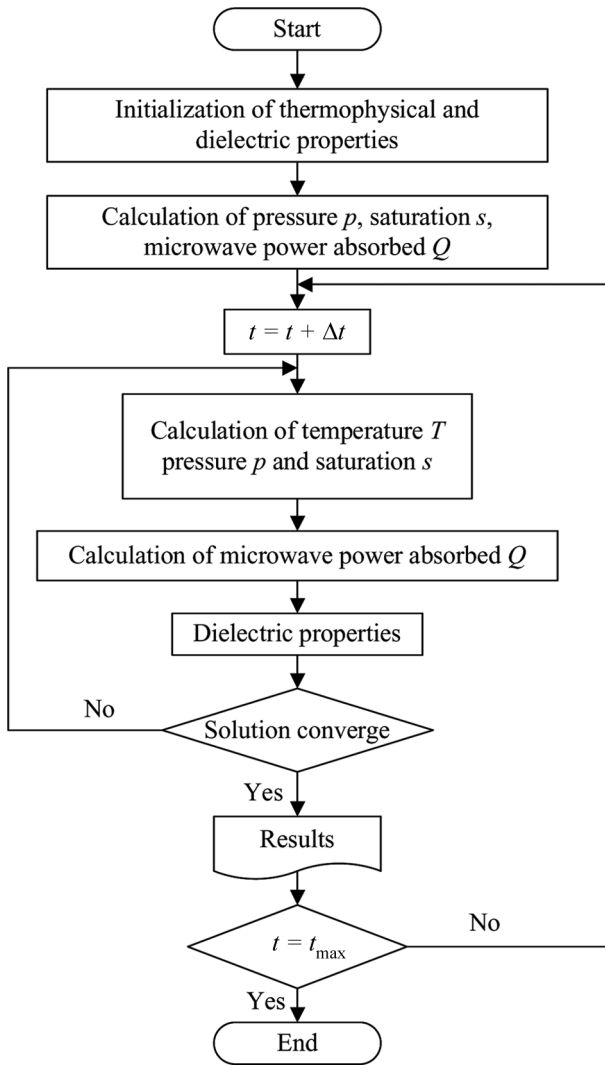
The details of computational scheme and strategy for solving the discretized transport equations (Eqs. (40)–(42)) are illustrated in Fig. 4. For numerical validation, the present numerical results are validated against the
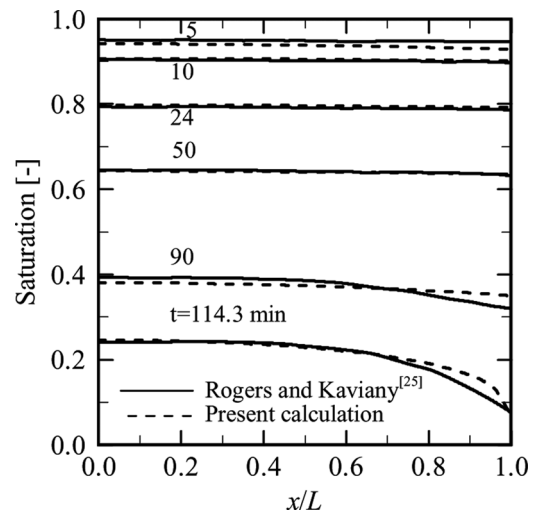

FIG. 4.   Computer scheme.

FIG. 5.   Saturation profile at various times: (a) results of Rogers and Kaviany; (b) present results.

results obtained by Rogers and Kaviany[25] in convective heating of an initially partially saturated packed bed problem. Figure 5 shows the numerical results from Rogers and Kaviany, and the present numerical results. It is observed that the trends of results are in good agreement. However, at longer times (114.3 min) the present saturation profile gradually declines at the unheated surface from x/L of 0.7 onwards; this discrepancy may be attributed to the additional conditions.

RESULTS AND DISCUSSION
The Effect of Vacuum Pressure

The numerical results for heat, multiphase flow, and pressure build-up in an unsaturated porous packed bed (composed of water, glass beads, and air) subjected to microwave energy are investigated at vacuum pressure of 13.3 kPa (100 torr) compared with atmospheric pressure condition. However, two drying processes using the operating microwave frequency of 2.45 GHz, the electric field intensity of 4,200 V/m, initial temperature of 25°C, initial moisture content of 0.5, and particle size of 0.15 mm are selected. The selected vacuum pressure of 13.3 kPa is in the typical range of pressure (1.33–26.66 kPa) for vacuum processing,[2] and is similar to Changrue[29] in which microwave vacuum processing is applied to investigate drying of carrot cubes. The input electric field intensity of 4,200 V/m is also lower than the critical breakdown electric field. Therefore, the effect of gas breakdown does not appear in this drying condition.

Figure 6 shows temperature profile at various times in the case of vacuum and atmospheric pressure. In contrast to that in a conventional drying, a microwave drying

provides higher temperature inside the drying sample while the surface temperature stays colder due to the effect of surrounding air. At the same time, the evaporation takes place at the surface of the sample at lower temperature due to evaporative cooling. It is seen that the temperature profile within the sample rises up steadily in the early stages of drying. Due to the large initial moisture content, the skin depth heating effect causes a majority of the microwave to decay exponentially into the sample according to Lambert's law, resulting in a lower rate of absorbed microwave power in the interior. As the drying process proceeds, moisture content is removed from the sample; the microwave can penetrate further into the sample as the material dries. During this state of drying, the temperature profile slows down considerably because moisture inside the sample is significantly reduced, reducing the dielectric loss factor as well as the absorbed microwave power. Nevertheless, temperature profiles at vacuum pressure are lower than atmospheric pressure, as shown in Fig. 7, because the boiling point of water falls under vacuum condition. It is found that at vacuum pressure of 13.3 kPa, water evaporation takes place within the sample and the temperature of the sample is always lower than the boiling point of water, which is equal to 56°C. Consequently, the sample processing temperature can be significantly lower than the atmospheric condition.

Figure 8 shows the absorbed microwave power profile in the case of vacuum and atmospheric pressure; it can be seen that the maximum of absorbed microwave power occurs at a depth of 2 cm and decreases with increasing the elapsed time. As the drying process proceeds, it would eventually cause the average moisture content to decrease and lead to decreased absorbed microwave power. The absorbed microwave power is directly affected by dielectric properties as a function of temperature and moisture content. The
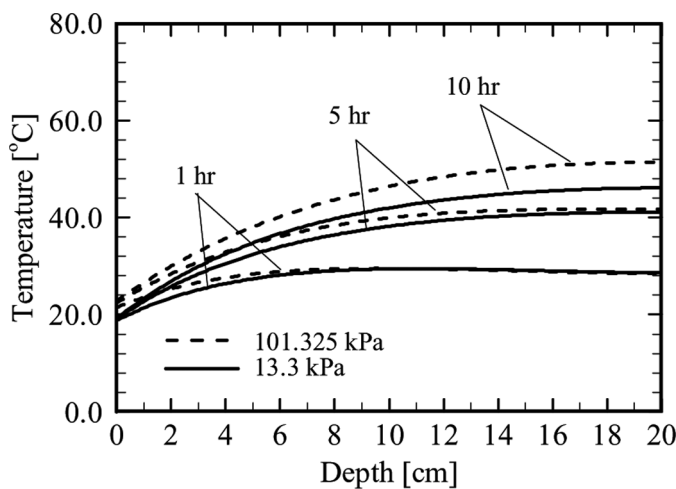

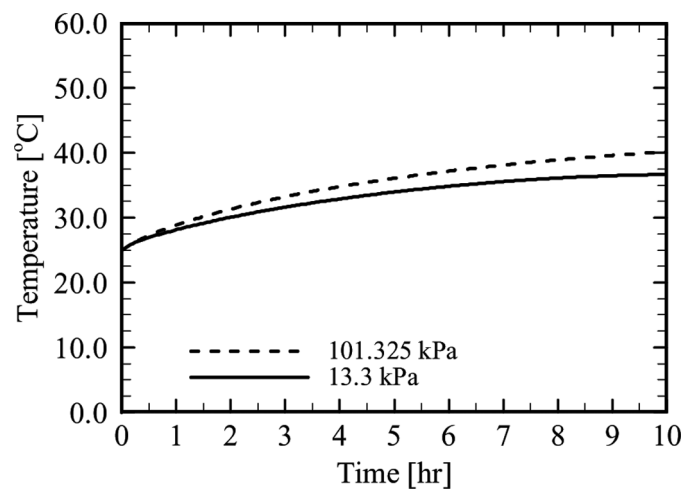FIG. 6. Temperature profile at various times ($d = 0.15$, mm, $E_0 = 4,200$ V/m, $s_0 = 0.5$).

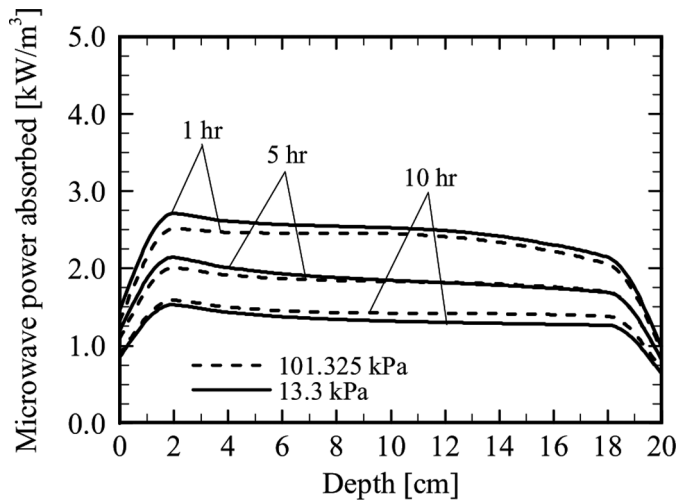FIG. 7. Temperature profile at depth of 6 cm ($d = 0.15$ mm, $E_0 = 4,200$ V/m, $s_0 = 0.5$).

FIG. 8. Absorbed microwave power profile at various times ($d = 0.15$ mm, $E_0 = 4,200$ V/m, $s_0 = 0.5$).

dielectric loss coefficient is significantly decreased with increasing temperature (further details shown in Ratanadecho et al.[22]). Therefore, the absorbed microwave power, atmospheric pressure is lower than vacuum pressure because of atmospheric pressure corresponding to a higher temperature profile.

Figure 9 presents the moisture profile at vacuum and atmospheric pressure. In the early state of drying, the internal movement of moisture is due to liquid flow by capillary action and vapor flow by molecular diffusion. As the drying process proceeds, the capillary action plays an important role in the moisture migration mechanism and maintains a good supply of liquid to the surface, and would cause the average moisture content inside the sample to decrease. However, at long stages of drying (10 h), the vapor diffusion
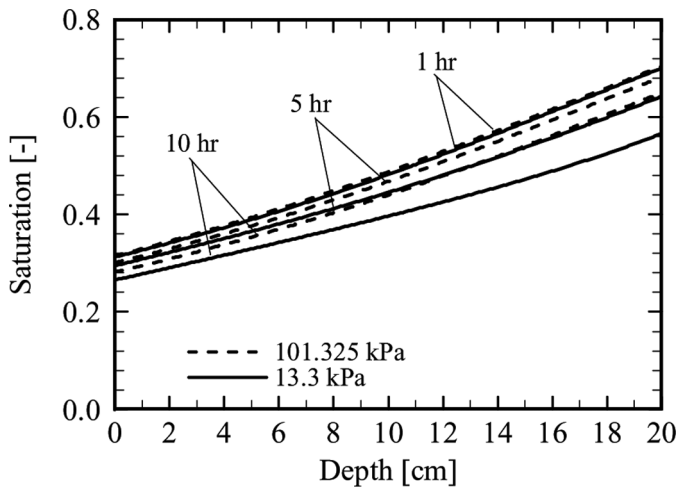

FIG. 9. Saturation profile at various times ($d = 0.15$, mm, $E_0 = 4,200$ V/m, $s_0 = 0.5$).

effect plays an important role in the moisture migration mechanism because of the sustained evaporation that is generated within the sample. The observed moisture profiles in the case of vacuum pressure are lower than atmospheric pressure for the following reasons. First, vacuum processing provides the lower boiling point and the higher absorbed microwave power to increase the rate of the water evaporation, and so causes moisture to transport upward. Second, vapor flow is greatly improved by increased total pressure gradients, and the effective molecular mass diffusion and binary mass diffusion (as displayed in Eqs. (16) and (17)). Finally, liquid flow is grown by capillary pressure.

Figure 10 shows total pressure distribution within the sample in the case of vacuum and atmospheric pressure drying conditions. As the drying process proceeds, total pressure is rapidly built up within the sample and is increasingly contributed to by the amount of accumulated vapor owing to the high diffusive vapor flux. It is seen that high temperature and pressure gradient are generated within the sample during the constant rate period. As a result, the capillary action plays an important role in the moisture migration
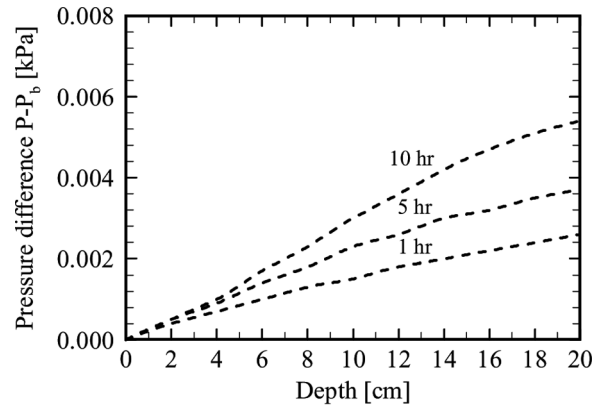
(a)
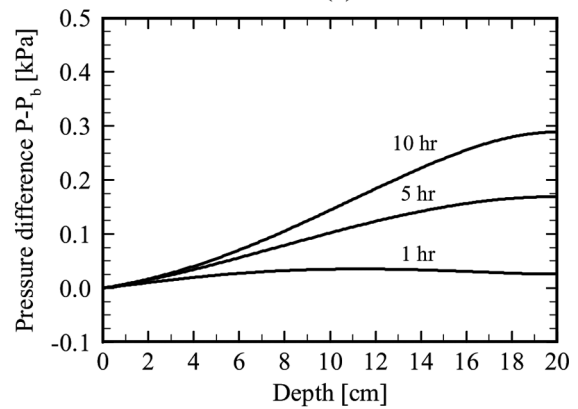
(b)

FIG. 10. Pressure distribution at various times ($d = 0.15$ mm, $E_0 = 4,200$ V/m, $s_0 = 0.5$): (a) atmospheric pressure; (b) vacuum pressure of 13.3 kPa.
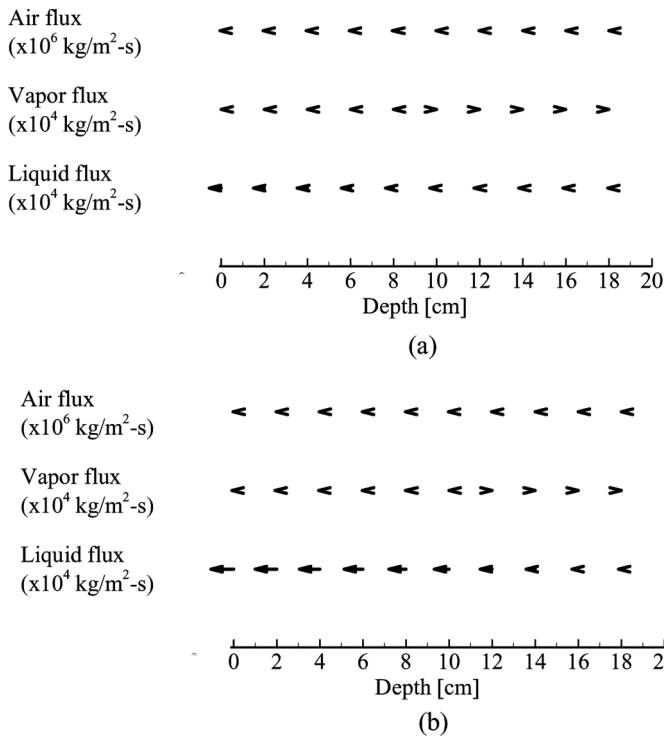
FIG. 11. Fluid movement patterns at 1 h ($d = 0.15$ mm, $E_0 = 4,200$ V/m, $s_0 = 0.5$): (a) atmospheric pressure; (b) vacuum pressure of 13.3 kPa.

FIG. 12. Fluid movement patterns at 5 h ($d = 0.15$ mm, $E_0 = 4,200$ V/m, $s_0 = 0.5$): (a) atmospheric pressure; (b) vacuum pressure of 13.3 kPa.

FIG. 13. Fluid movement patterns at 10 h ($d = 0.15$ mm, $E_0 = 4,200$ V/m, $s_0 = 0.5$): (a) atmospheric pressure; (b) vacuum pressure of 13.3 kPa.

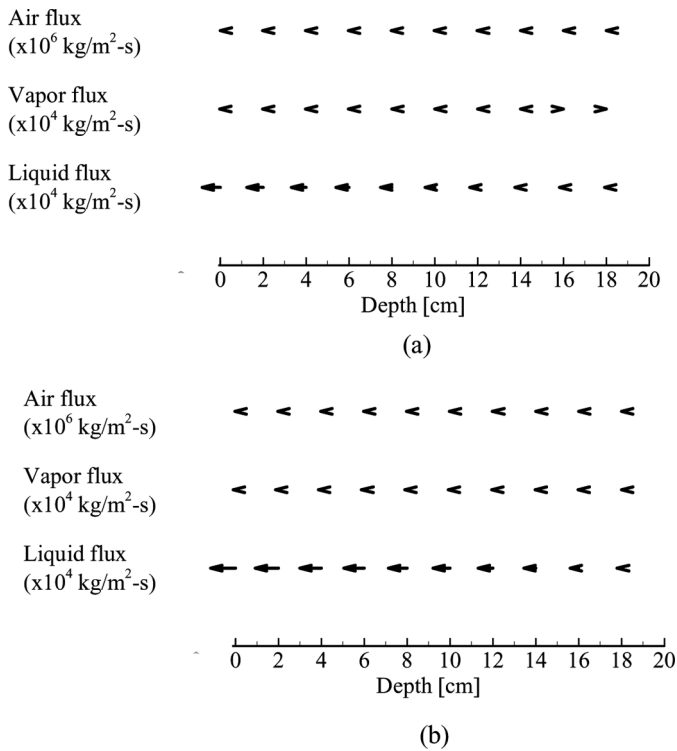mechanism, and maintains a good supply of liquid to the surface. The pressure gradients in terms of pressure difference are shown in Fig. 10; it was found that microwave vacuum drying allows a higher pressure gradient than atmospheric condition. This is because water evaporation inside the sample is accelerated by the higher absorbed microwave power at the lower boiling point of water.

In order to get more insight into the fluid transport, it is important to investigate the fluid movements within the sample in depth. The liquid flux, vapor flux, and air flux profiles in the case of vacuum and atmospheric pressure at drying times of 1 h, 5 h, and 10 h are shown in Figs. 11–13, respectively. It can be seen that the vapor flux flows within the sample toward the surface, and water evaporation takes place inside the sample and on the surface. As the drying process proceeds, the vapor flux flows in both directions at drying time of 5 h, but it flows in the same direction at drying time of 10 h because the vapor throughout the sample migrates in the direction of decreasing saturation.

The air flux moves toward the heated surface with a lower than the vapor flux because the air diffusion is decreased by the convective air flux, whereas the vapor diffusion is enhanced by the convective vapor flux. As the rate of liquid supply to the surface becomes lower, the water evaporation rate leading to the void volume is increased, thus allowing air flows away from the heated surface toward
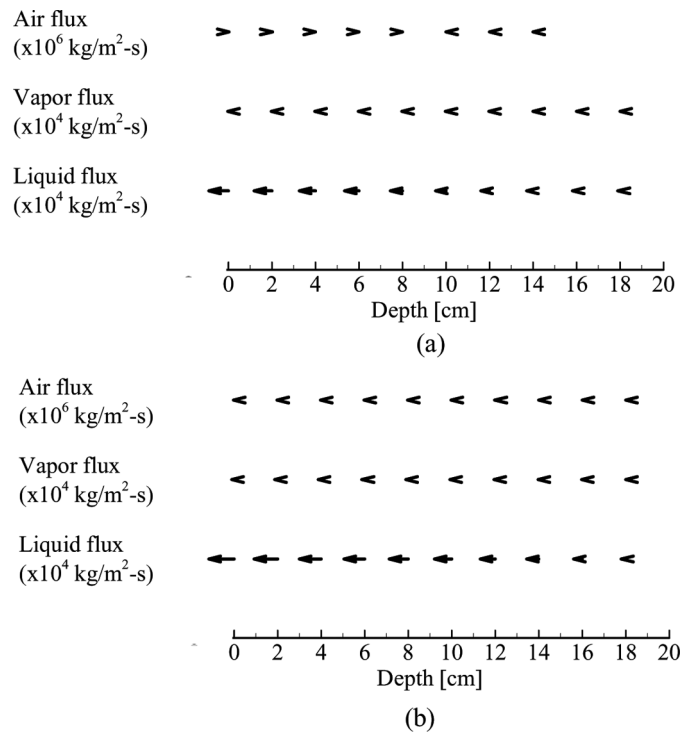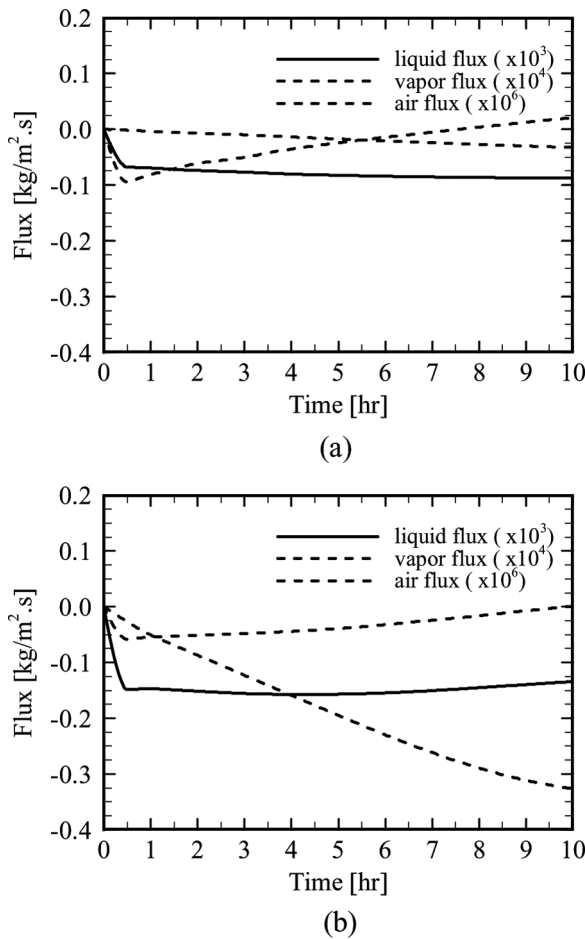
FIG. 14. Flux profile at depth of 6 cm ($d = 0.15$ mm, $E_0 = 4,200$ V/m, $s_0 = 0.5$): (a) atmospheric pressure; (b) vacuum pressure of 13.3 kPa.

the other surface. For the liquid flux, it can be observed that almost all of the liquid has migrated toward the upper surface of the sample due to capillary pressure and gas pressure build-up, which are simultaneously changed due to the effect of saturation and temperature distribution in each time period. The results of all flux profiles in the case of vacuum pressure are greater than atmospheric pressure because water evaporation within the sample is accelerated

TABLE 3
Electromagnetic and thermophysical properties used in the computations

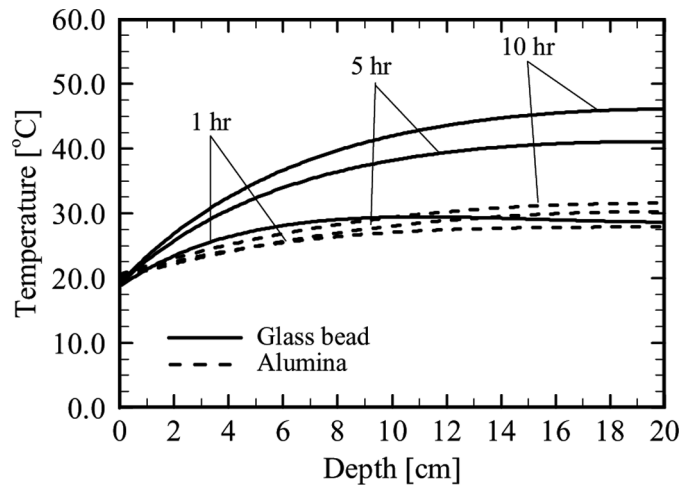| Properties	Air	Water	Glass bead	Alumina
ε'_r	1.0	$f(T)$	5.1	10.8
$\tan\delta$	0.0	$f(T)$	0.01	0.0145
μ_r	1.0	1.0	1.0	1.0
ρ	1.205	1000.0	2500.0	3750.0
C_p	1.007	4.186	0.8	1.046
λ	0.0262	0.610	1.0	26.0

FIG. 15. Temperature profile at various times of various particles ($d = 0.15$ mm, $E_0 = 4,200$ V/m, $s_0 = 0.5$, $P = 13.3$ kPa).

by the lower boiling point of water together with higher absorbed microwave power, and a high pressure gradient is generated.

Figure 14 illustrates the evolution of the flux profiles at depth of 6 cm in the case of vacuum and atmospheric pressure. In the case of vacuum pressure, the quantity of vapor flux is also higher than atmospheric pressure because it corresponds to higher pressure gradient, microwave power absorbtion, and rate of water evaporation.

The Effect of Type of Solid Particle

This section focuses on the effect of solid phase types, such as glass beads and alumina, whose electromagnetic and thermophysical properties are illustrated in Table 3. The numerical results for heat, multiphase flow, and pressure build-up in an unsaturated porous packed bed at various
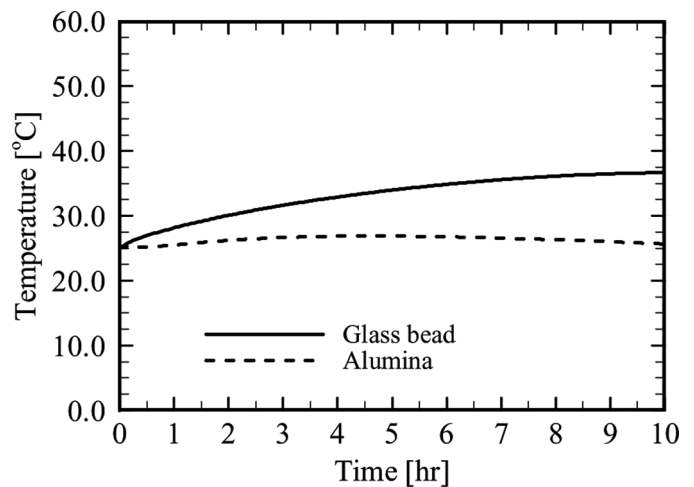

FIG. 16. Temperature profile at depth of 6 cm of various particles ($d = 0.15$ mm, $E_0 = 4,200$ V/m, $s_0 = 0.5$, $P = 13.3$ kPa).
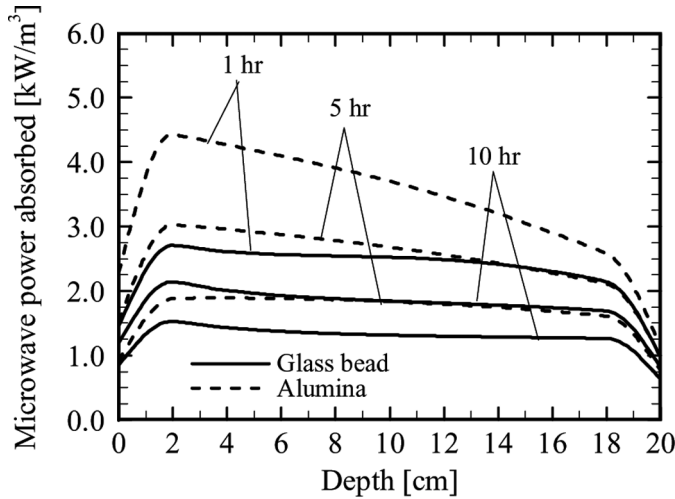
FIG. 17.   Absorbed microwave power profile at various times of various particles ($d = 0.15$ mm, $E_0 = 4,200$ V/m, $s_0 = 0.5$, $P = 13.3$ kPa).

solid particle types subjected to microwave energy using the operating microwave frequency of 2.45 GHz are investigated at vacuum pressure of 13.3 kPa (100 torr), electric field intensity of 4,200 V/m, initial temperature of 25°C, and initial moisture content of 0.5, as well as particle size of 0.15 mm.

Figures 15 and 16 show temperature profile at various times and depth of 6 cm, respectively, and Fig. 17 illustrates the absorbed microwave power within the sample in the case of alumina. It is seen that the absorbed microwave power is greater than in the case of glass beads (as shown in Fig. 8), because alumina have higher dielectric properties, as displayed in Table 3. However, temperature profiles in the case of alumina are lower than for glass beads because the heat capacitance of alumina is greater than that

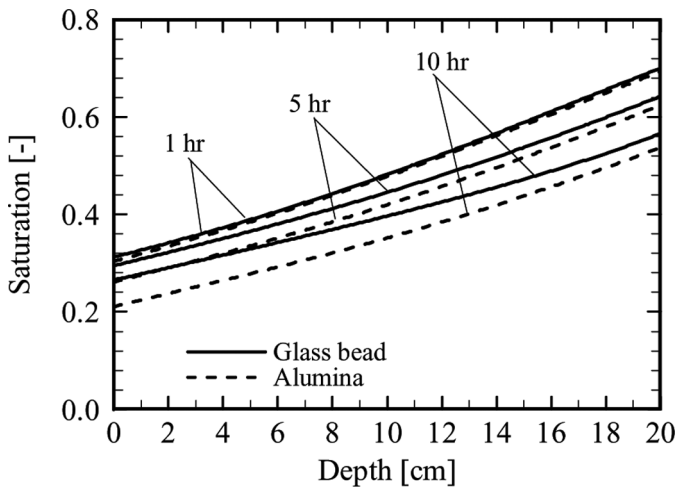FIG. 18.   Saturation profile at various times of various particles ($d = 0.15$ mm, $E_0 = 4,200$ V/m, $s_0 = 0.5$, $P = 13.3$ kPa).
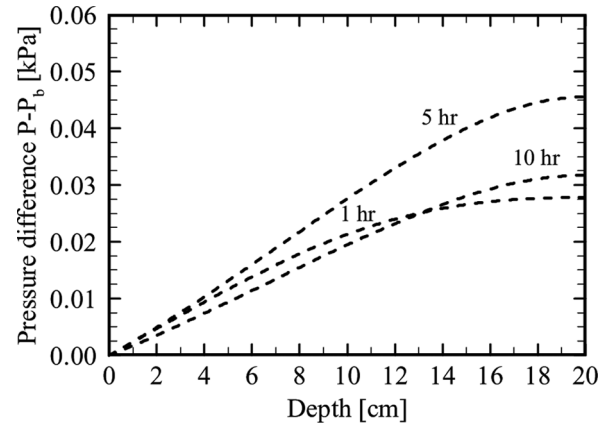

FIG. 19.   Pressure distribution at various times of alumina ($d = 0.15$ mm, $E_0 = 4,200$ V/m, $s_0 = 0.5$, $P = 13.3$ kPa).
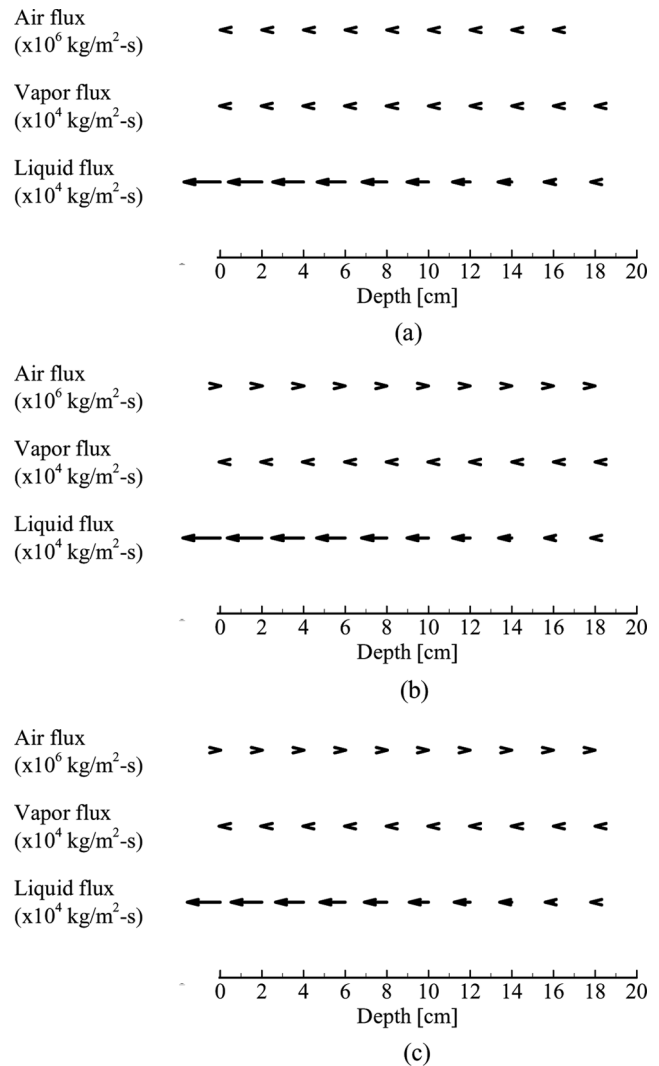

FIG. 20.   Fluid movement patterns of alumina ($d = 0.15$ mm, $E_0 = 4,200$ V/m, $s_0 = 0.5$, $P = 13.3$ kPa): (a) 1 h; (b) 5 h; (c) 10 h.
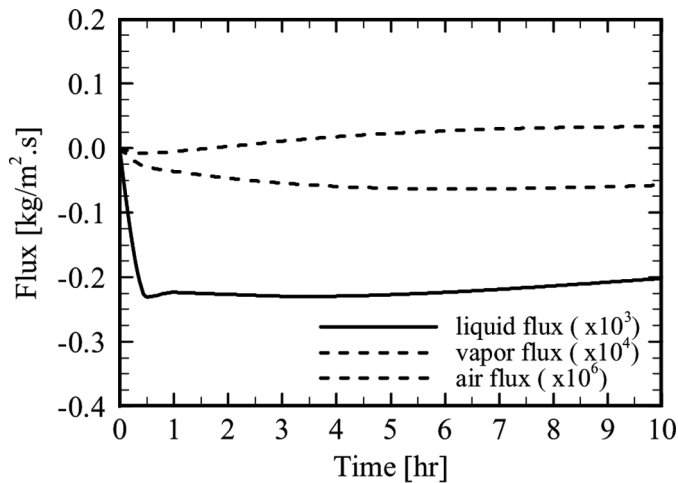
FIG. 21.   Flux profile at depth of 6 cm of alumina ($d = 0.15$ mm, $E_0 = 4,200$ V/m, $s_0 = 0.5$, $P = 13.3$ kPa).

of glass beads. Furthermore, it is found that the saturation profile, illustrated in Fig. 18, is lower than that in the case of glass beads.

Figure 19 shows pressure difference profile within the sample in the case of alumina. Total pressure is lower than in the case of glass beads because it is possible to have lower temperature profiles taking place inside the sample.

Figure 20 illustrates fluid movement patterns inside the sample in the case of alumina at various times such as 1, 5, and 10 h. For fluid transport phenomena, liquid, vapor, and air flux are explained in the previous subsection. It is observed that liquid flux within the sample is greater compared with glass beads (as shown in Figs. 11(b), 12(b), and 13(b)). Additionally, liquid flux profile at a depth of 6 cm is also greater than in the case of glass beads, as can be seen in Fig. 21.

This study shows the capability of the numerical analysis to handle heat–mass transport and pressure build-up in a one-dimensional porous medium subjected to a microwave vacuum drying problem. With further quantitative validation of the present method, this method can be used as a tool for investigating in detail this particular microwave drying under vacuum pressure of phase change in an unsaturated porous media at a fundamental level.

CONCLUSIONS

The numerical analysis presented describes many important interactions within the sample (as an unsaturated porous media) during microwave vacuum drying. A generalized mathematical model for analysis of heat and mass transfer, and pressure build-up in the sample subjected to microwave energy, can be used successfully to describe transport phenomena under vacuum pressure condition. The vacuum pressure significantly influences temperature,

absorbed microwave power, saturation and pressure build-up distribution, and movement of fluid inside the sample. In this work, the microwave energy absorbed was assumed to decay exponentially into the sample, according to Lambert's law. This assumption is valid for the large dimensions of the sample as considered in the study. For a small sample, the spatial variations of the electromagnetic field and microwave energy absorbed within the sample must be obtained by a completed solution of the unsteady Maxwell's equations. The next step, numerical analysis of heat–mass transport and pressure build-up in a two-dimensional unsaturated porous medium subjected to a combined microwave and vacuum system, will be investigated. However, these results provide understanding into the vacuum drying of a porous medium subjected to electromagnetic energy which can be applied in industrial drying.

NOMENCLATURE

c	Velocity of light (m/s)
C_p	Specific heat capacity (J/kg K)
D	Binary mass diffusion (m^2/s)
D_m	Effective molecular mass diffusion (m^2/s)
E	Electromagnetic field intensity (V/m)
f	Frequency of the microwave (Hz)
g	Gravitational constant (m/s^2)
H_v	Specific heat of evaporation (J/kg)
h_c	Heat transfer coefficient (W/m^{2}K)
h_m	Mass transfer coefficient (m/s)
J	Leverett functions
K	Permeability (m^2)
Le	Lewis number
M	Molecular weight (kg/mol)
$\dot{n}$	Phase change term (kg/m^{3}s)
P	Microwave power (W)
p	Pressure (Pa)
p_{vs}	Partial pressure of the saturation vapor (Pa)
Q	Absorbed microwave power term (W/m^3)
R	Universal gas constant (J/mol K)
s	Water saturation
s_e	Effective water saturation
s_{ir}	Irreducible water saturation
T	Temperature ($^\circ$C)
t	Time (s)
u	Velocity (m/s)

Greek Letters

α	Attenuation constant
$\tan\delta$	Loss tangent coefficient
δ_s	Skin depth
ε	Complex permittivity (F/m)
ε'	Permittivity or dielectric constant
ε''	Dielectric loss factor
ϕ	Porosity
λ_{eff}	Effective thermal conductivity (W/m K)

μ	Magnetic permeability (H/m) or Dynamic viscosity (Pa s)
ρ	Density (kg/m^3)
σ	Gas-liquid interfacial tension

Subscripts

0	Free space
a	Air
c	Capillary
g	Gas
l	Liquid
p	Particle
r	Relative
v	Water vapor
z	Cartesian coordinate

ACKNOWLEDGMENT

REFERENCES

1. Mujumdar, A.S. *Handbook of Industrial Drying*, 2nd Ed.; Marcel Dekker: New York, 1995.
2. Metaxas, A.C.; Meridith, R.J. *Industrial Microwave Heating*; Peter Peregrinus Ltd.: London, 1983.
3. Datta, A.K.; Anantheswaran, R.C. *Handbook of Microwave Technology for Food Applications*; Marcel Dekker: New York, 2001.
4. Perré, P.; Mosnier, S.; Turner I.W. Vacuum drying of wood with radiative heating: I. Experimental procedure. *AIChE Journal* **2004**, *50*, 97–107.
5. Jomaa, W.; Baixeras, O. Discontinuous vacuum drying of oak wood: Modelling and experimental investigations. *Drying Technology* **1997**, *15*(9), 2129–2144.
6. Drouzas, A.E.; Schubert, H. Microwave application in vacuum drying of fruits. *Journal of Food Engineering* **1996**, *28*, 203–209.
7. Drouzas, A.E.; Tsami, E.; Saravacos, G.D. Microwave/vacuum drying of model fruit gels. *Journal of Food Engineering* **1999**, *39*, 117–122.
8. Péré, C.; Rodier, E. Microwave vacuum drying of porous media: Experimental study and qualitative considerations of internal transfers. *Chemical Engineering and Processing* **2002**, *41*, 427–436.
9. Sunjka, P.S.; Rennie, T.J.; Beaudry, C.; Raghavan, G.S.V. Microwave-convective and microwave-vacuum drying of cranberries: A comparative study. *Drying Technology* **2004**, *22*(5), 1217–1231.
10. Hu, Q.; Zhang, M.; Mujumdar, A.S.; Xiao, G.; Sun, J. Drying of edamames by hot air and vacuum microwave combination. *Journal of Food Engineering* **2006**, *77*, 977–982.
11. Perré, P.; Turner, I.W. A 3-D version of TransPore: A comprehensive heat and mass transfer computational model for simulating the drying of porous media. *International Journal of Heat and Mass Transfer* **1999**, *42*, 4501–4521.
12. Rattanadecho, P.; Pakdee, W.; Stakulcharoen, J. Analysis of multiphase flow and heat transfer: Pressure buildup in an unsaturated porous slab exposed to hot gas. *Drying Technology* **2008**, *26*, 39–53.
13. Ni, H.; Datta, A.K.; Torrance, K.E. Moisture transport in intensive microwave heating of biomaterials: A multiphase porous media model. *International Journal of Heat and Mass Transfer* **1999**, *42*, 1501–1512.
14. Ratanadecho, P.; Aoki, K.; Akahori, M. A numerical and experimental investigation of the modeling of microwave drying using a rectangular wave guide. *Drying Technology* **2001**, *19*(9), 2209–2234.
15. Campañone, L.A.; Zaritzky, N.E. Mathematical analysis of microwave heating process. *Journal of Food Engineering* **2005**, *69*(3), 359–368.
16. Cha-Um, W.; Rattanadecho, P.; Pakdee, W. Experimental analysis of microwave heating of dielectric materials using a rectangular waveguide (MODE: TE10) (case study: water layer and saturated porous medium). *Experimental Thermal and Fluid Science* **2009**, *33*(3), 472–481.
17. Rattanadecho, P.; Suwannapum, N.; Cha-Um, W. Interactions between electromagnetic and thermal fields in microwave heating of hardened type I-cement paste using a rectangular waveguide (influence of frequency and sample size). *ASME Journal of Heat Transfer* **2009**, *131*, 082101–082112.
18. Hansson, L.; Antti, L. Modeling microwave heating and moisture redistribution in wood. *Drying Technology* **2010**, *26*, 552–559.
19. Jia, D.; Afzal, M.T. Modeling the heat and mass transfer in microwave drying of white oak. *Drying Technology* **2008**, *26*, 1103–1111.
20. Sungsoontorn, S.; Rattanadecho, P.; Pakdee, W. One-dimensional model of heat and mass transports and pressure buildup in unsaturated porous materials subjected to microwave energy. *Drying Technology* **2011**, *29*, 189–204.
21. Suwannapum, N.; Rattanadecho, P. Analysis of heat–mass transport and pressure buildup induced inside unsaturated porous media subjected to microwave energy using a single (TE10) mode cavity. *Drying Technology* **2011**, *29*, 1010–1024.
22. Ratanadecho, P.; Aoki, K.; Akahori, M. Experimental and numerical study of microwave drying in unsaturated porous material. *International Communications in Heat and Mass Transfer* **2001**, *28*, 605–616.
23. Wang, J.; Schmugge, T. An empirical model for the complex dielectric permittivity of soil as a function of water content. *IEEE Transactions on Geosciences and Remote Sensing* **1980**, *18*, 288–295.
24. Von Hippel, A.R. *Dielectric Materials and Applications*; MIT Press: Boston, 1954.
25. Rogers, J.A.; Kaviany, M. Funicular and evaporative-front regimes in convective drying of granular beds. *International Journal of Heat and Mass Transfer* **1992**, *35*(2), 469–479.
26. Kaviany, M.; Mittal, M.; Torrance, K.E. Funicular state in drying of a porous slab. *International Journal of Heat and Mass Transfer* **1987**, *30*, 1407.
27. Watanuki, J. Fundamental study of microwave heating with rectangular wave guide. M.S. thesis, Nagaoka University of Technology, Japan, 1998.
28. Patankar, S.V. *Numerical Heat Transfer and Fluid Flow*; McGraw-Hill: New York, 1980.
29. Changrue, V. Hybrid (osmotic, microwave-vacuum) drying of strawberries and carrots. Ph.D. thesis, Macdonald Campus of McGill University, Canada, 2006.